





Simultaneous three-dimensional elemental mapping of Hollandite and Pyrochlore material phases in ceramic waste form materials

Peter Joseph C. Damian¹ | Alex P. Cocco¹ | Jacob A. Wrubel¹ | Tao Hong² | Rajendra K. Bordia²  | Yijin Liu³  | Piero Pianetta³ | Jake W. Amoroso⁴ | Kyle S. Brinkman²  | Wilson K. S. Chiu¹ 

¹Department of Mechanical Engineering, University of Connecticut, Storrs, Connecticut

²Department of Materials Science and Engineering, Clemson University, Clemson, South Carolina

³Stanford Synchrotron Radiation Lightsource, SLAC National Accelerator Laboratory, Menlo Park, California

⁴Savannah River National Laboratory, Aiken, South Carolina

Correspondence

Kyle S. Brinkman, Department of Materials Science and Engineering, Clemson University, Clemson, SC.

Email: ksbrink@clemson.edu and

Wilson K. S. Chiu, Department of Mechanical Engineering, University of Connecticut, Storrs, CT.

Email: wchiu@engr.uconn.edu

Funding information

US Department of Energy Nuclear Energy University Program, Grant/Award Number: DE-NE0008260; U. S. Department of Energy, Grant/Award Number: DE-AC09-08SR22470

Abstract

Differential X-ray absorption contrast tomography was performed on model ceramic composite systems to image the 3D spatial distributions of Ga and Nd containing phases. The model material systems were fabricated such that they contained two constituent phases. Ga-doped Ba hollandite ($\text{Ba}_{1.33}\text{Ga}_{2.66}\text{Ti}_{5.34}\text{O}_{16}$), and pyrochlore ($\text{Nd}_2\text{Ti}_2\text{O}_7$) which are under consideration as nuclear waste immobilization matrices. Two complementary techniques have been used to characterize the 3D distribution of phases. The analysis suggests that the 3D spatial distributions of hollandite and pyrochlore can be readily identified through the distributions Ga and Nd, respectively. These results represent a critical development towards characterizing the complex microstructure inherent to practical materials such as multiphase ceramic composite waste forms. Moreover, these methods can be applied to elucidate microstructural features that fundamentally determine the performance and properties of complex systems, which is central to the design of durable waste forms as well as many other real materials such fuel cells, batteries, ultra-high temperature ceramics.

KEYWORDS

hollandite, nuclear waste, pyrochlore, waste form, X-ray computed tomography, X-ray methods

1 | BACKGROUND

1.1 | Ceramic waste form materials

Crystalline ceramics have been under development and consideration as matrices for immobilizing nuclear waste constituents for the past four decades and continue to be researched as an alternative to the most widely adapted technology, which uses vitrification into borosilicate glass as a means of waste immobilization.¹ Waste immobilization using glass is

advantageous as for large volume waste streams in which industrial-scale vitrification is commonplace and demonstrated in the nuclear industry using simple glass fabrication techniques.² Additionally, glasses have resilience to alpha radiation damage, and are able to accommodate both a relatively large number of different elements as well as some compositional uncertainty, which is unavoidable owing to analytical accuracies used to characterize the waste. However, glasses are susceptible to degradation and leaching of their matrix constituents; a condition that is exacerbated when exposed

to water at high temperatures and pressures (300–400°C, 300–1000 bar^{1,3,4}) that is expected in geologic disposal. These anticipated geologic conditions result in the dissolution of the glass.^{1,3}

Ceramic waste forms are another means of nuclear waste immobilization that have the potential to offer improved performance at reduced cost compared to glass waste forms.⁵ Ceramic waste forms consist of multiple crystalline phases (hollandite, pyrochlore, perovskite, etc) which generally target specific waste constituents and are designed to emulate the crystal structures of naturally occurring minerals.^{1,5} For example, hollandite and perovskite are incorporated to preferentially encapsulate the waste elements, cesium and strontium, respectively.¹ In contrast to glass-based waste forms, ceramic waste forms exhibit greater stability when exposed to hydrothermal conditions.⁵ Furthermore, minerals containing radioactive elements found in the earth's crust and dated to several hundred thousand years substantiates the geologic stability of ceramic waste forms.³ This research is focused on two principal phases which represent a majority of the crystalline phases in most formulations: Ga-doped Ba hollandite, and neodymium titanate, a pyrochlore structure.⁶

Because ceramic waste forms are often compared to glass waste forms, they are also often designed as a multiphase assemblage for similarly complex waste streams (ie, legacy wastes with diverse chemistry) in which four or more discrete phases might be targeted in the final waste form. However, more simple, single and double-phase systems can be used to reduce the experimental resources needed for critical measurements of the more complex systems, and themselves, could be expected to become favorable for immobilization of unique wastes as ceramic waste forms continue to gain prominence. This initial work focused on two principal phases that represent the majority of the crystalline phases in formulations represented in the literature: Ga-doped Ba hollandite, and neodymium titanate, a pyrochlore structure.⁶

Ga-doped Ba hollandite ($\text{Ba}_{1.33}\text{Ga}_{2.66}\text{Ti}_{5.34}\text{O}_{16}$), one of the ceramic phases studied in this experiment has been, and is being, investigated for its potential to immobilize Cs from waste streams. The hollandite crystal structure is tunnel-like in nature, inside which Cs is incorporated.^{7,8} Ga lowers the melting temperature of the hollandite and produces beneficial X-ray absorption characteristics, which can be exploited for interrogation of the microstructure.⁹

The other ceramic phase examined in this work was $\text{Nd}_2\text{Ti}_2\text{O}_7$, which adopts a monoclinic structure. While many 3+ cations adopt the pyrochlore structure in the correct stoichiometry, Nd was chosen as representative since it is the most prevalent lanthanide element found in many waste stream compositions and it too possesses readily accessible X-ray absorption characteristics.^{6,10} Pyrochlores of various compositions are typically considered to contain many of the transuranic elements.^{11–13}

The ultimate performance measure of any waste form is its resistance to leaching other transport mechanisms; that is, durability.⁵ In order to design a waste form with improved durability, it is necessary to understand the material's microstructural properties that influence the performance and durability of a given material.⁹ The primary microstructural properties of interest in ceramic waste forms include phase composition, morphology, and porosity. In order to elucidate these properties, methods are needed that possess the requisite capability and resolution to determine feature sizes at the sub-micron dimension.

1.2 | Differential X-ray absorption contrast tomography

Numerous three-dimensional imaging techniques have been developed to characterize materials used in energy-related technologies.⁹ Improving current ceramic waste form designs hinges on the characterization of their microstructure to understand these materials' performance for the intended application. The 3D imaging technique selected to analyze these materials must be able to (a) image dense, high Z, materials, (b) identify multiple phases, (c) discern 3D spatial distributions of each phase, and (d) characterize microstructural features of small scale, 10's to 100's of nanometers. Focused ion beam-scanning electron microscopy (FIB-SEM serial) sectioning and synchrotron-based X-ray nanotomography (XNT) fulfill these requirements.^{9,14}

FIB-SEM is a destructive 3D imaging technique, relying on the continuous SEM imaging of a sample's surface and removal of the imaged surface via milling with a FIB in the form of thin slices of material (10's of nm thick). Two-dimensional spatial resolution for this technique is determined by the SEM's resolution, which is often single to tens of nanometers. The resolution of the depth is dependent on the thickness of the milled slices.^{9,15–18}

X-ray nanotomography is a non-destructive 3D imaging technique relying on the use of a synchrotron to provide monochromatic X-rays (X-rays with a single energy level) at sufficient intensity to allow for high spatial resolutions (10's of nanometers). Additionally, the use of a synchrotron enables the energy level of the X-rays to be "tuned" to specific energy levels, which is critical for elemental sensitivity.⁹

Elemental sensitivity for X-ray nanotomography is possible through the use of absorption edges. Typically, X-ray absorption decreases with an increase of X-ray energy level, however at element-specific energy levels, X-ray absorption drastically increases; this is called an "absorption edge".¹⁹ As each absorptivity increase is element-specific, it is possible to select X-ray energies above and below these absorption edges to use to image a sample. Then, using both sets of images, it is possible

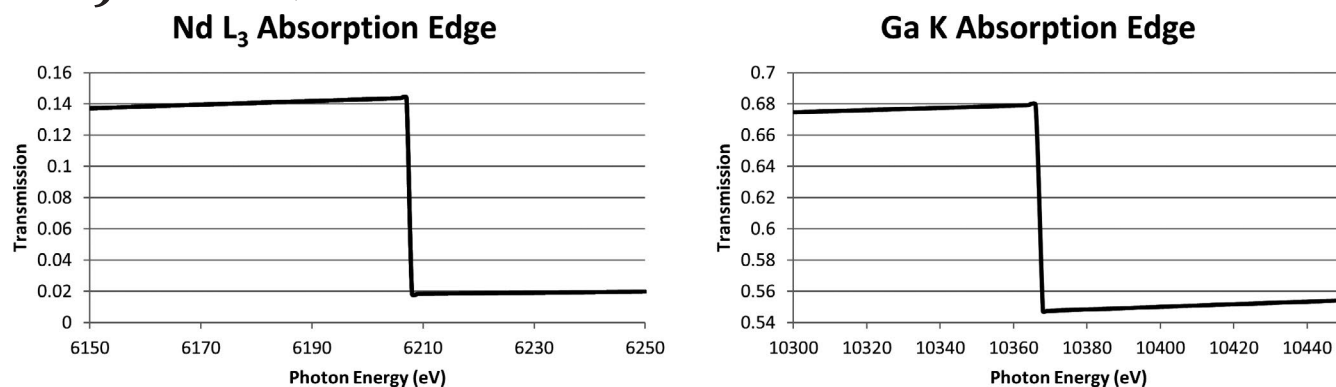


FIGURE 1 Nd L₃ and Ga K absorption edges predicted using the CXRO calculator²¹

to map specific elements, and subsequently phases, within a sample by subtracting the above absorption edge image from the below absorption edge image.^{20,21} Elemental sensitivity was demonstrated in a previous study for *Ni only* in a porous SOFC anode consisting of Ni and YSZ. Ni was identified in this material by imaging the Ni-YSZ sample using monochromatic X-rays 16 eV below and 24 eV above the Ni K absorption edge at 8.333 keV.²⁰ This technique is known as differential X-ray absorption contrast tomography (DXACT).¹⁴

The primary difference between X-ray nanotomography and DXACT is that X-ray nanotomography is performed multiple times using X-rays at different energy levels for DXACT. These energy levels are strategically selected to enable elemental sensitivity. Thus, DXACT shares all benefits associated with performing traditional X-ray nanotomography. The advantage unique to DXACT is that elemental information is obtained using contrast alone. A notable disadvantage is the reliance on a synchrotron X-ray source. In some instances the intensity of X-rays used to image the sample may not be consistent resulting in imaging artifacts, where background noise is greater in the “above” absorption edge image. This phenomenon is addressed by the image segmentation procedure.

Nd₂Ti₂O₇ (pyrochlore) and Ba_{1.33}Ga_{2.66}Ti_{5.34}O₁₆ (hollandite) were examined in this experiment. The Ga K absorption edge at 10.37 keV and the Nd L₃ absorption edge at 6.21 keV were used in this experiment to determine the distribution of Ga and Nd within the samples. Using these elemental distributions, it is possible to identify the location of the hollandite and pyrochlore phases as Ga and Nd partition to these respective phases. Further distinctions between phases can be made using concentration, which corresponds to contrast

(see Figure 5 and Table 3). The validity of this method was demonstrated in a previous work, in which a Ga-doped Ba hollandite (Ba_{1.33}Ga_{2.66}Ti_{5.34}O₁₆) was imaged using this form of X-ray tomography.¹⁴

It is important to note that it is possible to predict the change in transmission of X-rays through a given sample using the Center for X-ray Optics (CXRO) calculator. This tool predicts the transmission drop of X-rays for a slab of material of a specified composition.²² As the chemical composition of the model waste forms are known, this tool provides X-ray transmission drops characteristic for elements present in the sample. Figure 1 presents the calculated transmission change across the Ga and Nd absorption edges predicted from the CXRO calculator.

2 | EXPERIMENT

2.1 | Sample preparation

Three different model ceramic waste form were studied, (a) single phase Nd₂Ti₂O₇ (pyrochlore), (b) single phase Ba_{1.33}Ga_{2.66}Ti_{5.34}O₁₆ (hollandite), and (c) a composite sample consisting of a 50:50 (volume percent) pyrochlore-hollandite mixture. Additionally, the density was varied for the composite samples to levels between 70 and 95 percent relative density. Gradients in density are known to occur during large scale waste form processing and will have an impact on the interfacial area available for surface reactions leading to elemental release.²³ Table 1 summarizes the samples studied by type, composition, number of samples, and density.

TABLE 1 Summary of all samples analyzed using differential X-ray absorption contrast tomography

	Composition	Number of samples	Density	Calculations
Single phase	Nd ₂ Ti ₂ O ₇	2	-	X-ray transmission
	Ba _{1.33} Ga _{2.66} Ti _{5.34} O ₁₆	2	-	
Multi-phase, 50:50	Nd ₂ Ti ₂ O ₇ :Ba _{1.33} Ga _{2.66} Ti _{5.34} O ₁₆	2	70%	Volume fraction, PSD
	Nd ₂ Ti ₂ O ₇ :Ba _{1.33} Ga _{2.66} Ti _{5.34} O ₁₆	2	95%	

The single-phase hollandite $\text{Ba}_{1.33}\text{Ga}_{2.66}\text{Ti}_{5.34}\text{O}_{16}$, and pyrochlore $\text{Nd}_2\text{Ti}_2\text{O}_7$ materials were synthesized by a traditional solid-state reaction method. Stoichiometric mixtures of BaCO_3 , Ga_2O_3 , Nd_2O_3 , and TiO_2 were ball milled in ethanol with ZrO_2 milling media for 24 hours. The powders were dried and calcined at 1200°C for 10 and 2 hours to form the hollandite and pyrochlore phases, respectively. Composite samples were fabricated by mixing single phase powders in the volume ratio of 50:50, followed by ball milling in ethanol with ZrO_2 milling media for 24 hours. Sintered pellets were prepared by pressing the composites (100 MPa) into green pellets and followed by sintering at 1300°C for 30 minutes to achieve 95% density or 1250°C for 2 hours to achieve 70% density.

The phase structure was characterized by X-ray diffraction (Rigaku TTR-III) analysis using Cu K radiation (D/Max-gA) with 2θ from 10 to 70 degree at a scan rate of 0.2 degrees per minute. The morphology of hollandite sample was observed using a scanning electron microscope (SEM, Hitachi SU-6600). The chemical composition was confirmed by energy dispersive spectrometer (EDS, Hitachi SU-6600).

2.2 | Transmission X-ray microscopy

The model ceramic waste form materials were milled into cylindrical samples approximately $15\ \mu\text{m}$ in diameter and height using a Xe plasma FIB. The samples were mounted onto watch

pins via a Pt weld which were placed in the TXM in Beamline 6-2 at the Stanford Synchrotron Radiation Lightsource (SSRL). The $\text{Nd}_2\text{Ti}_2\text{O}_7$ samples were imaged above (6.241 keV) and below (6.175 keV) the Nd L_3 -absorption edge ($\sim 6.21\ \text{keV}$). The $\text{Ba}_{1.33}\text{Ga}_{2.66}\text{Ti}_{5.34}\text{O}_{16}$ samples were imaged above (10.4 keV) and below (10.334 keV) the Ga K-absorption edge ($\sim 10.37\ \text{keV}$). The samples containing both materials were imaged above and below both the Nd L_3 and Ga K-absorption edges. Voxel sizes for the images taken at 6.175, 6.241, 10.334, and 10.4 keV were 24.1, 24.3, 40.3, and 40.5 nm, respectively. TXM Wizard, a software package developed at SSRL, was used for image processing and reconstruction.²⁴ ImageJ and Avizo were used for the purposes of image segmentation and 3D visualization respectively. Details of the segmentation procedure can be found in the Supplemental Materials.

3 | RESULTS AND DISCUSSION

Figure 2 displays the surface morphology of the 95% dense composite sample and the corresponding elemental EDS mapping results. In the SEM backscatter (BSE) image, two phases can be distinguished. A comparison of the SEM results with the EDS mapping results revealed darker, grey grains were the hollandite phase $\text{Ba}_{1.33}\text{Ga}_{2.66}\text{Ti}_{5.34}\text{O}_{16}$ and the that the light colored grains corresponded to the pyrochlore phase $\text{Nd}_2\text{Ti}_2\text{O}_7$.

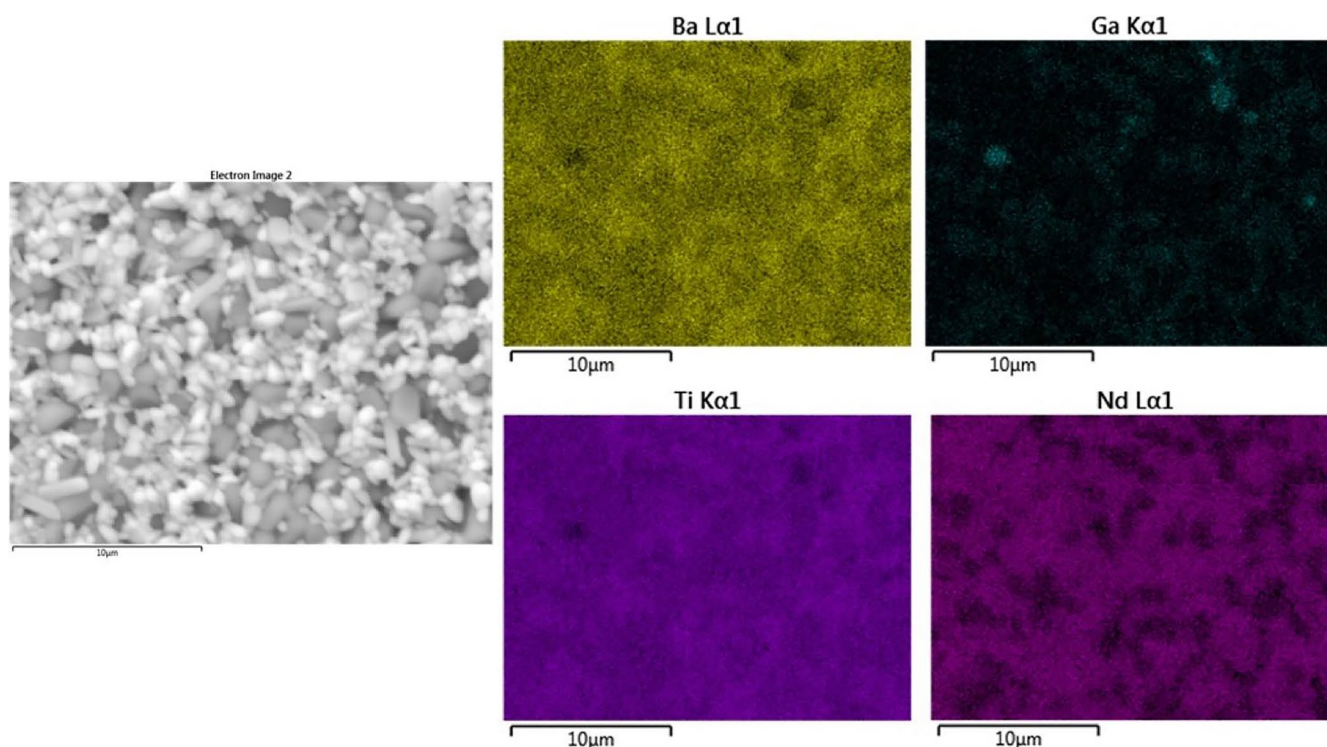


FIGURE 2 Backscatter SEM image with Ba, Ga, Ti and Nd element EDS mapping result for 95% density $\text{Ba}_{1.33}\text{Ga}_{2.66}\text{Ti}_{5.34}\text{O}_{16}$ - $\text{Nd}_2\text{Ti}_2\text{O}_7$ sample. Ga mapping result also indicates some Ga hotspots [Colour figure can be viewed at wileyonlinelibrary.com]

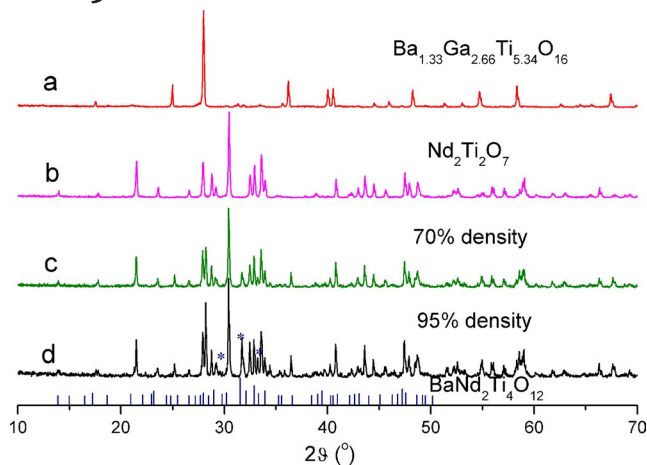


FIGURE 3 XRD spectrum for (A) pure $\text{Ba}_{1.33}\text{Ga}_{2.66}\text{Ti}_{5.34}\text{O}_{16}$, (B) pure $\text{Nd}_2\text{Ti}_2\text{O}_7$, that were synthesized at 1200 for 10 h and 3 h separately, and (C,D) the composite phase of $\text{Ba}_{1.33}\text{Ga}_{2.66}\text{Ti}_{5.34}\text{O}_{16}$ and $\text{Nd}_2\text{Ti}_2\text{O}_7$ (volume fraction 50:50) with a density of 95% and 70%. The standard XRD peaks (JADE PDF#44-0061) for potential emergent phase Ba-Nd-Ti-O ($\text{BaNd}_2\text{Ti}_4\text{O}_{12}$) is also included as a reference [Colour figure can be viewed at wileyonlinelibrary.com]

Figure 3 displays the XRD patterns for the $\text{Ba}_{1.33}\text{Ga}_{2.66}\text{Ti}_{5.34}\text{O}_{16}$, $\text{Nd}_2\text{Ti}_2\text{O}_7$, and 50:50 dual phase mixtures with 70% and 95% density. $\text{Ba}_{1.33}\text{Ga}_{2.66}\text{Ti}_{5.34}\text{O}_{16}$ and $\text{Nd}_2\text{Ti}_2\text{O}_7$ both are well crystallized with hollandite and pyrochlore separately as indicated in Figure 3A-B. The dual phase samples of $\text{Ba}_{1.33}\text{Ga}_{2.66}\text{Ti}_{5.34}\text{O}_{16}$ and $\text{Nd}_2\text{Ti}_2\text{O}_7$ with the volume fraction of 50:50 sintered at 1250 and 1300 with 70% and 95% density both showed minor additional peaks in addition to the primary hollandite and pyrochlore phases. In Figure 3, the peaks at 31.7° and 33.2° two theta suggests the formation of third phase resulting from reactions between $\text{Ba}_{1.33}\text{Ga}_{2.66}\text{Ti}_{5.34}\text{O}_{16}$ and $\text{Nd}_2\text{Ti}_2\text{O}_7$ starting materials during the sintering process. The chemical composition and crystal structure are uncertain, however preliminary structural matches with the XRD database (JADE PDF#44-0061) including known elements present in the sample suggest Ba-Nd-Ti-O phase such as $\text{BaNd}_2\text{Ti}_4\text{O}_{12}$ as a likely emergent phase.

3.1 | TXM results for baseline Pyrochlore ($\text{Nd}_2\text{Ti}_2\text{O}_7$)

Figure 4 shows the cross sections of a single-phase, baseline pyrochlore sample imaged below (panel A, 6.175 keV) and above (panel B, 6.241 keV) the Nd L_3 absorption edge (~ 6.21 keV). Panel C highlights the contrast change generated from imaging across this absorption edge, and panel D displays the resulting segmentation of the cross sectional image. Two distinct regions can be identified in the segmentations of the pyrochlore samples, namely a region containing pyrochlore, and the pores and background. The segmentation results are consistent with this expectation and establish the baseline behavior of the $\text{Nd}_2\text{Ti}_2\text{O}_7$ on its own.

3.2 | TXM results for baseline Hollandite ($\text{Ba}_{1.33}\text{Ga}_{2.66}\text{Ti}_{5.34}\text{O}_{16}$)

Figure 5 shows the cross sections of a baseline hollandite sample imaged below and above (panels A and B) the Ga K-absorption edge (~ 10.37 keV). A secondary phase was identified in both hollandite samples, denoted by the lighter regions in panels B and C and the black regions in panel D. These regions exhibited a much higher contrast change across the absorption edge when compared to the bulk of the material, denoting a higher concentration of Ga compared to the majority of the sample. These observations are consistent with previous work with this material which concluded that these regions of higher Ga concentration originate from the use of excess Ga as a dopant to obtain maximum contrast change across the Ga absorption edge. Essentially, during the synthesis of these baseline samples, due to the excessive amounts of Ga present as a dopant, a new Ga-Rich phase forms as seen in Figure 5.¹⁴

3.3 | Baseline sample measurement validation

As a form of validation, the transmission of X-rays through the samples was measured for one pyrochlore and one

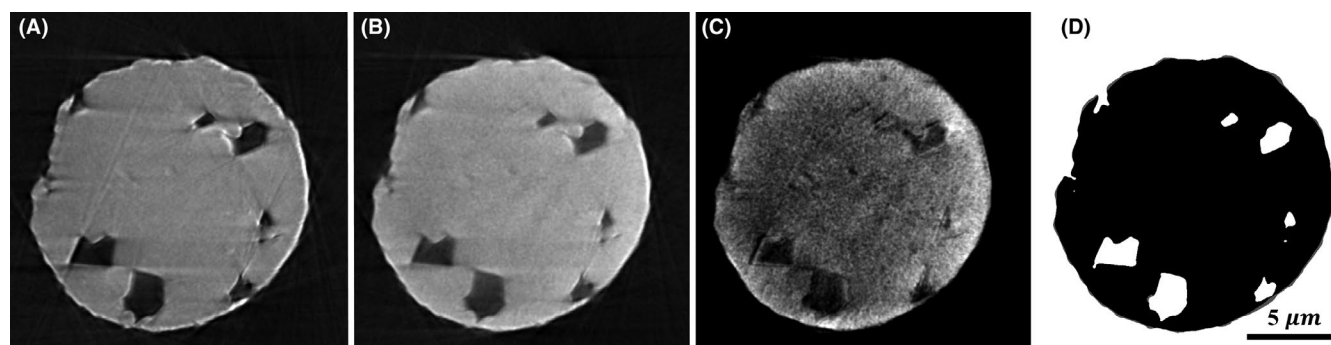


FIGURE 4 Cross sections of single-phase, baseline pyrochlore sample. A, Below absorption edge image, 6.175 keV. B, Above absorption edge image, 6.241 keV. C, Contrast change across absorption edge. D, Segmented dataset

TABLE 2 Average voxel intensities and measured % transmission change for a pyrochlore sample

Region	X-ray energy levels		% transmission change	
	6.175 keV	6.241 keV	% Change	Predicted % change
Pyrochlore	110.4	124.5	12.7	12
Background	87.8	87.2	0	-

hollandite baseline sample. This measurement was performed by sampling multiple regions within specific phases visually identified throughout the baseline samples, and taking the average voxel intensity values. The first two columns in Tables 2 and 3 present the average voxel intensity values for every phase. The percent transmission change was then calculated by taking the difference between the above and below edge average voxel intensity values and is listed in the third column of Tables 2 and 3. The percent transmission change was calculated according to the equation below:

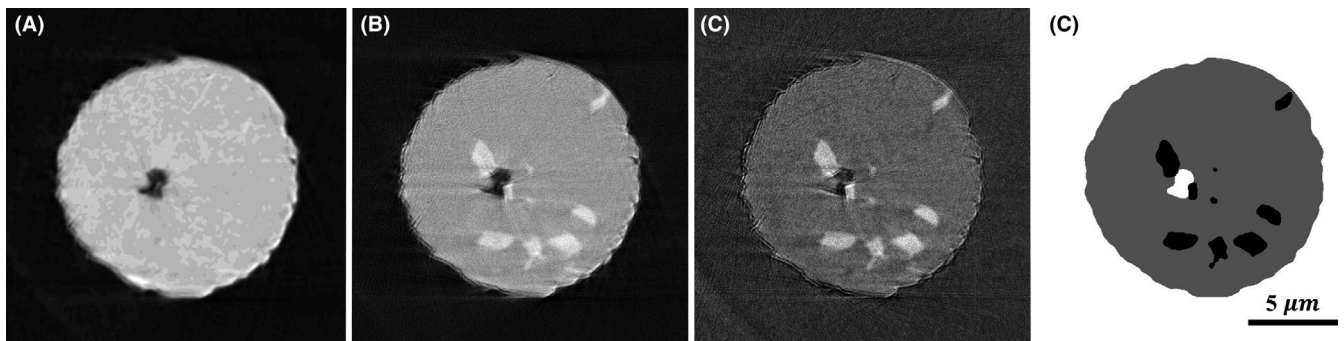
$$\% \Delta_i = \frac{A - B}{B} - \% \Delta_{\text{background}} \quad (1)$$

The $\% \Delta_i$ is the percent transmission change for phase i and A is the average voxel intensity value for the above edge image, and B is the average voxel intensity value for the below edge image. The $\% \Delta_{\text{background}}$ is the percent transmission change for the background samples. The predicted transmission changes listed in the last column of Tables 2 and 3 was calculated through the use of the CXRO calculator.

Table 2 presents the average voxel intensities (columns 1 and 2), measured transmission change (column 3), and

predicted transmission change (column 4) for the baseline pyrochlore sample. One solid region was identified, pyrochlore, which exhibited a transmission change, 12.7%, that agrees reasonably well with the predicted transmission change of 12%. This agreement suggests that DXACT can be used to accurately image samples consisting of $\text{Nd}_2\text{Ti}_2\text{O}_7$.

Table 3 presents the average voxel intensities (columns 1 and 2), measured transmission change (column 3), and predicted transmission change (column 4) for the baseline hollandite sample. Two solid phases were identified within this material, the hollandite phase and a “Ga-Rich” phase. The CXRO calculator was used to predict the transmission change for the hollandite material for the DXACT measurement. As the secondary “Ga-Rich” phase is a result of the bulk material synthesis procedure, the predicted transmission change does not account for the formation of this secondary phase, explaining the discrepancy between the measured and predicted transmission change for the hollandite phase. The small transmission change for the hollandite phase suggests that it may not be easily identifiable when using DXACT to image the more complicated mixed samples. As the “Ga-Rich” phase exhibits a much larger transmission

**FIGURE 5** Cross section of baseline hollandite sample. A, Below absorption edge image, 10.334 keV. B, Above absorption edge image, 10.4 keV. C, Contrast change across absorption edge. D, Segmented cross section**TABLE 3** Average voxel intensities and measured % transmission change for a hollandite sample

Region	X-ray energy levels		% transmission change	
	10.334 keV	10.4 keV	% change	Predicted % change
Hollandite	68.1	81.2	2.7	13
Ga-Rich	68.4	87.9	11.9	-
Background	53.7	62.6	0	-

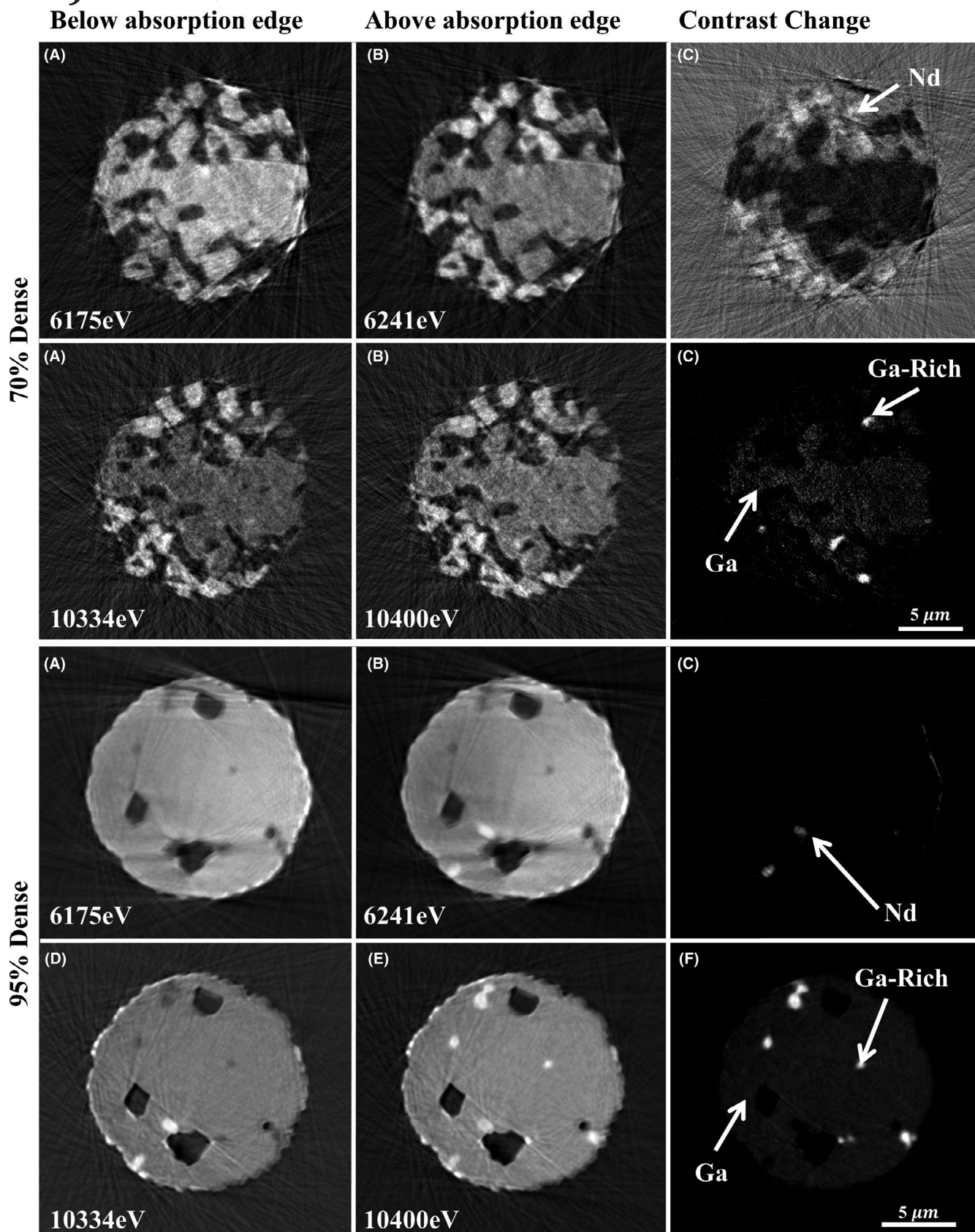


FIGURE 6 Cross sections of 70% and 95% dense samples. A, Below Nd L_3 absorption edge (6.175 keV). B, Above Nd L_3 absorption edge (6.241 keV). C, Contrast change across Nd L_3 absorption edge. D, Below Ga K absorption edge (10.334 keV). E, Above Ga K absorption edge (10.4 keV). F, Contrast change across Ga K absorption edge

change, it should be more easily characterized using DXACT when compared to the hollandite phase.

As mentioned previously, as the concentration of a given element in the sample increases, the magnitude of the contrast change (or % transmission change) across an absorption edge increases. The primary hollandite phase identified in the baseline hollandite samples exhibits a much smaller transmission change of 2.7%, when compared to the transmission change of the Ga-Rich phase of 11.9%. Therefore, this suggests that the Ga-Rich phase contains more Ga than the hollandite phase.

3.4 | $\text{Nd}_2\text{Ti}_2\text{O}_7\text{:Ba}_{1.33}\text{Ga}_{2.66}\text{Ti}_{5.34}\text{O}_{16}$: composite samples

In addition to the baseline samples, differential X-ray absorption contrast tomography was applied to four, 50:50, pyrochlore: hollandite samples of two distinct densities, 70% and 95% dense. From the results of the baseline samples, three distinct phases are expected, pyrochlore, hollandite, and a Ga-Rich phase which exhibits a much higher contrast change across the Ga K-absorption edge than the hollandite material.

Figure 6 presents the cross sections of a 70% and 95% dense, 50:50 pyrochlore: hollandite waste form material imaged below (panel A) and above (panel B) the Nd L_3 – absorption edge and below (panel D) and above (panel E) the Ga K – absorption edge. This multi-phase system contains three distinct phases identified by the arrows in panel

C, which presents the contrast change across each absorption edge. One Nd-containing phase and two Ga-containing phases were identified across their respective absorption edges, consistent with the behaviors of the baseline samples. These three phases were consistently identified in all 70% and 95% dense samples.

Figure 7 presents the three-dimensional microstructures of a 70% dense (panels A and B) and a 95% dense (panels C and D) hollandite-pyrochlore waste form obtained using DXACT. All three phases are presented in panels A and C as teal, gold, and magenta which correspond to the pyrochlore, hollandite, and Ga-Rich regions as identified in Figure 6 and the baseline samples. Panels B and D depict solely the hollandite and Ga-Rich regions to aid in visualization of these phases.

3.5 | FIB validation

The imaging data were collected using a FEI dual-beam 400-S FIB system (Hitachi). The FIB milling was performed with a Ga^+ ion-beam at a current of 460 pA at 30 kV. For SEM imaging, a magnification of 12kX and a through the Lens Detector operating in Backscatter Electron (BSE) mode at a low scan rate were employed. Data processing followed the steps of (a) alignment of the consecutive slices, (b) correction of the dimensions taking into account the tilt of the electron beam, (c) thresholding of the grey levels and labeling of phases, and (d) 3D image generation. The remaining drift

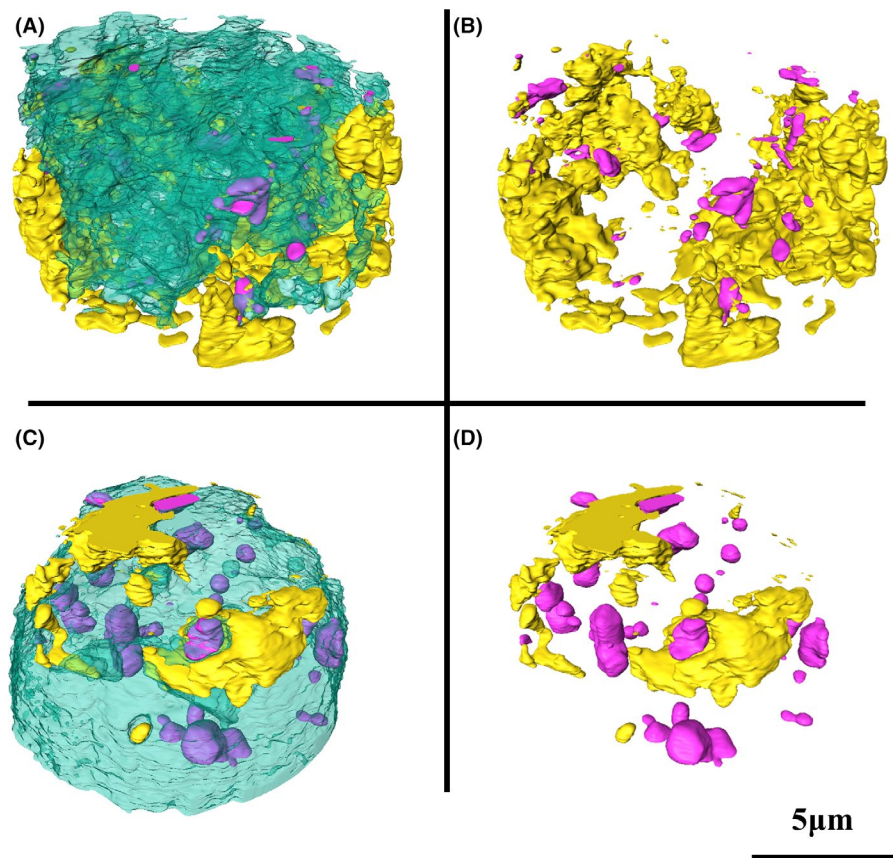


FIGURE 7 3D visualization of a 70% dense (panels A and B) and 95% dense (panels C and D) multiphase ceramic waste form. Three phases are readily identifiable in panels A and C; teal, gold, and magenta represent pyrochlore, hollandite, and Ga-Rich regions, respectively [Colour figure can be viewed at wileyonlinelibrary.com]

components of the electron beam in the x and y directions were corrected by applying least square fitting algorithms to achieve image alignment. Finally, the resulting volume was cropped to retain the features common to all slices. The absolute dimensions in the x direction were obtained from a calibrated SEM magnification.

A section of approximately $10 \times 10 \times 10 \mu\text{m}$ was removed from the bulk material and an ex-situ slice and view technique was applied to obtain a sequence of 214 images. The volume fractions of each phase and their corresponding grain size distribution across the volume were determined. Figure 8A,B and C depict the 3D structure of the phases identified as (a) $\text{Ba}_{1.33}\text{Ga}_{2.66}\text{Ti}_{5.34}\text{O}_{16}$, (b) $\text{Nd}_2\text{Ti}_2\text{O}_7$, and (c) Ba-Nd-Ti-O phase which was preliminary identified and subsequently referred to as $(\text{BaNd}_2\text{Ti}_4\text{O}_{12})$. The total 3D structure is presented in Figure 8D. The volume fractions calculated from 3D data provided the following results: 39.02% ($\text{Ba}_{1.33}\text{Ga}_{2.66}\text{Ti}_{5.34}\text{O}_{16}$), 46.63% ($\text{Nd}_2\text{Ti}_2\text{O}_7$), and 14.55% (Ba-Nd-Ti-O). The quality of individual images demonstrates the advantage of the lift-out technique. The lift-out technique provides a low resistance path to ground which greatly reduces the negative effects of charging. The particle size distribution of each phase is shown in Figure 9.

3.6 | Volume fraction validation

As a form of validation, the volume fractions for each phase identified with differential absorption contrast tomography were calculated. From sample preparation and characterization, the composition and density of each sample is known. The volume fraction of each phase, pyrochlore, hollandite, and Ga-Rich is calculated for all mixed samples. Table 4 presents each phase's volume fraction in percentages for each sample and the average between both samples first for the 95% dense samples, and then for the 70% dense samples. For the 95% dense samples, the pyrochlore and hollandite containing phases are each expected to contribute 47.5% of the samples' volume. Similarly, for the 70% dense samples, the pyrochlore and hollandite containing phases are each expected to contribute 35% of the samples' volume. The volume fraction of the pores is expected to contribute the remaining "volume" of the samples.

It is clear from the results presented in Table 4, that individual hollandite-pyrochlore mixed samples are comprised largely of one phase. For example, the first 95% dense sample consists mostly of hollandite, whereas the second 95% dense sample is comprised mainly of pyrochlore. This is also apparent in Figure 7, where the samples contain

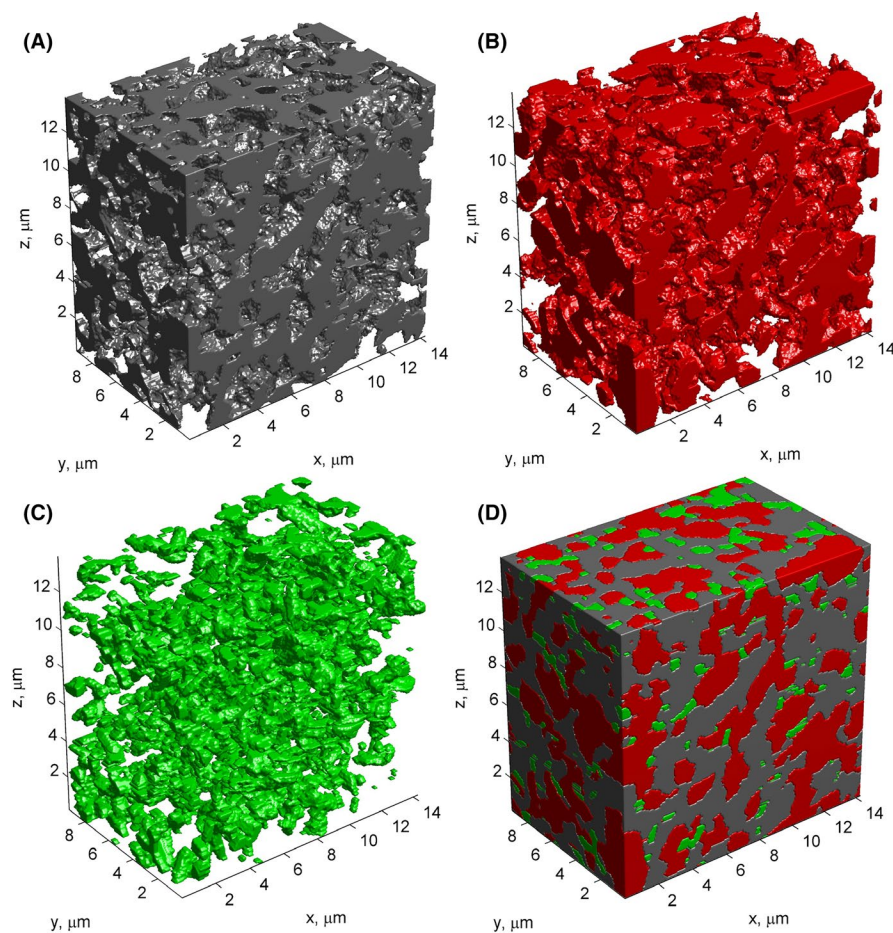


FIGURE 8 3D structure of (A) $\text{Ba}_{1.33}\text{Ga}_{2.66}\text{Ti}_{5.34}\text{O}_{16}$, (B) $\text{Nd}_2\text{Ti}_2\text{O}_7$ phase, (C) Ba-Ga-Nd-Ti-O, and (D) the spatial distribution of each phase in bulk. The structure is derived from in-situ FIB-SEM images [Colour figure can be viewed at wileyonlinelibrary.com]

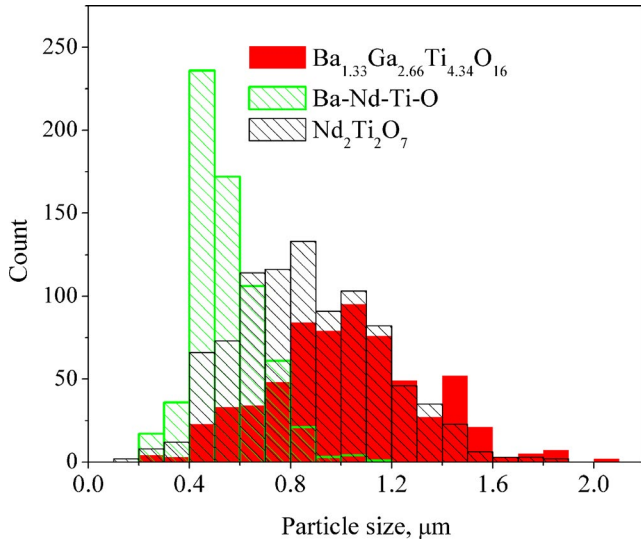


FIGURE 9 Particle size distribution of each phase derived from FIB 3D reconstruction [Colour figure can be viewed at wileyonlinelibrary.com]

primarily pyrochlore. The average volume fractions of the multiphase material at each density approach the expected volume fractions. For example, the average volume fractions of the 95% dense samples are 6.99% pore, 41.46% pyrochlore, 44.74% hollandite, and 5.22% Ga-Rich which approach the expected volume fractions of 5% pore, 47.5% pyrochlore, and 47.5% hollandite. This suggests that when the samples were prepared from the bulk material, that an uneven sampling process occurred. Essentially, when selecting regions of the bulk material to measure, regions containing mostly pyrochlore or hollandite were milled, resulting in the volume fractions observed above. This suggests that at the length scales measured, the phase distribution is not homogeneous, potentially affecting performance of these materials as particular phases leach out from the structure, removing waste and compromising structural integrity. However, all phases were clearly identified in these structures, demonstrating the feasibility of DXACT.

3.7 | Differential X-ray computed tomography particle size distributions

The particle size distributions (PSDs) obtained from the DXACT segmentations and visualized using characterization methods developed by Grew et al.^{25,26} are plotted in Figure 10. Alpha is related to the volume fraction of each respective phase such that total area beneath the PSD curves in Figure 10 represents that specific phase's volume fraction. For example, in panel A, the total area beneath the blue curve is the volume fraction of the Ga phase in this 70% dense sample.

From the volume fraction validation of both the 70% and 95% dense samples, individual samples were expected to consist of largely one element. This partitioning can be demonstrated by examining the PSDs. In Figure 10 panels A and C, Ga constitutes the majority of the microstructure for these samples, whereas Nd contributes the most volume to the samples in panels B and D.

Qualitatively, Figures 9 and 10 agree. Two major phases have been identified, pyrochlore and hollandite. Both of these major phases exhibit similar particle sizes respective to each measurement technique. Additionally, the emergent phases identified in each analysis, the Ga-Rich phase in DXACT, and the Ba-Nd-Ti-O phase in the FIB analysis are comprised of particles much smaller than that of the major phases. Particle sizes appear to be larger in the DXACT-obtained structures than the FIB 3D reconstructions. This difference can be partially explained due to the uneven sampling that occurred during sample preparation for the DXACT measurements in addition to differences in PSD characterization methods. In FIB 3D reconstruction, phase separation relies on SEM images contrast from BSE and EDX mapping. The phase boundaries between the emergent phase, Ba-Nd-Ti-O, $\text{Nd}_2\text{Ti}_2\text{O}_7$, and $\text{Ba}_{1.33}\text{Ga}_{2.66}\text{Ti}_{5.34}\text{O}_{16}$ may not be clearly distinguished, thus affecting the particle size distributions obtained from the SEM images in Figure 9.

TABLE 4 Volume fraction of each phase in all mixed samples for all densities listed in percentages. The average volume fractions are calculated for each phase. The 70% dense sample 2 corresponds to A/B in Figure 7. The 95% dense sample 2 corresponds to C/D in Figure 7.

Phase	95% dense			70% dense		
	Sample 1 volume fraction (%)	Sample 2 volume fraction (%)	Average volume fraction (%)	Sample 1 volume fraction (%)	Sample 2 volume fraction (%)	Average volume fraction (%)
Pore	4.61	9.36	6.99	29.44	41.67	35.56
Pyrochlore	0.19	82.74	41.46	10.55	46.57	28.56
Hollandite	84.64	4.84	44.74	52.45	9.65	31.05
Ga-Rich	10.39	0.05	5.22	4.71	0.84	2.77

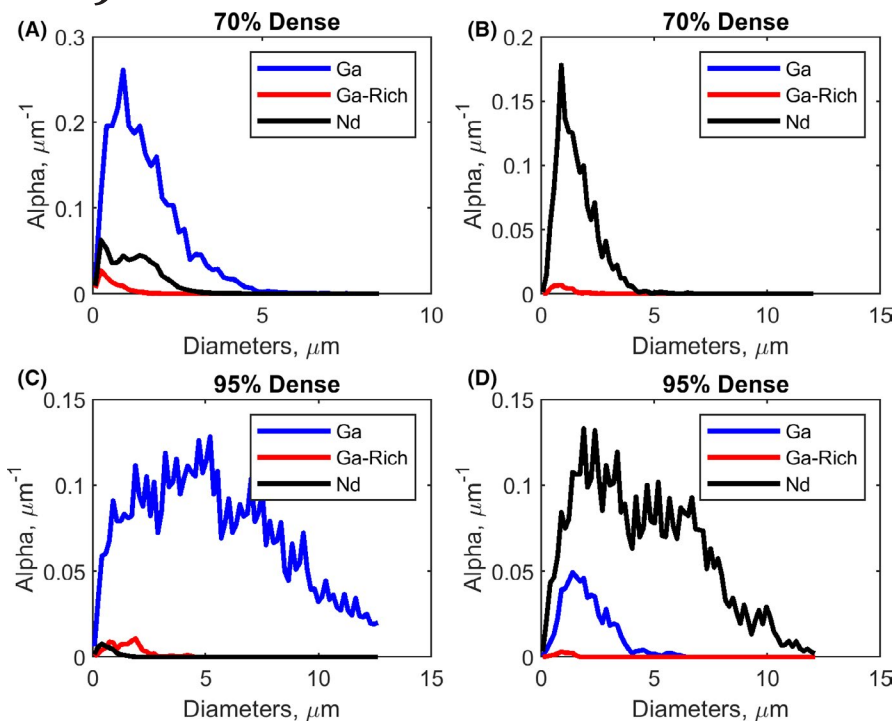


FIGURE 10 Particle size distribution obtained from DXACT segmentations. Panel A and B show the PSDs for each separate 70% dense sample. Panels C and D show the PSDs for each 95% dense sample [Colour figure can be viewed at wileyonlinelibrary.com]

4 | CONCLUSIONS

Differential X-ray absorption contrast tomography was performed on model ceramic waste form materials consisting of $\text{Nd}_2\text{Ti}_2\text{O}_7$ and $\text{Ba}_{1.33}\text{Ga}_{2.66}\text{Ti}_{5.34}\text{O}_{16}$ using the TXM in beamline 6-2 at SSRL. Several model waste form systems were considered, namely the pyrochlore and hollandite phases separately, and mixed pyrochlore: hollandite samples with varying porosities. This work has demonstrated that DXACT can be used to characterize these model materials consisting of *multiple ceramic waste forms* and identify distinct phases based on the relative concentrations of specific elements (Nd and Ga).

DXACT offers researchers in the field a nondestructive, 3D imaging technique capable of resolving multiple phases based on elemental distributions. This technique will be particularly useful in revealing information about the behavior of ceramic waste form microstructures when developing new ceramic waste form compositions or synthesis procedures. The results presented in this paper represent a critical step in the development of methods to characterize the elemental distribution and microstructure, and subsequently chemical and morphological behavior, of practical ceramic waste form systems.

ACKNOWLEDGMENTS

The authors are grateful for the support of Nuclear Energy University Program of the US Department of Energy Award ID: DE-NE0008260, CFA-14-6357: “A New Paradigm for Understanding Multiphase Ceramic Waste Form

Performance.” Portions of this research were carried out at the Stanford Synchrotron Radiation Lightsource, a national user facility operated by Stanford University on behalf of the U.S. Department of Energy, Office of Basic Energy Sciences. This work was supported in part by the award of a Thermo Fisher Scientific Graduate Fellowship to JAW. The FIB studies at the University of Connecticut were performed using the facilities in the UConn/Thermo Fisher Scientific Center for Advanced Microscopy and Materials Analysis (CAMMA). Work conducted at Savannah River National Laboratory was supported by the U.S. DOE under contract number DE-AC09-08SR22470. The engineering support from D. Van Campen, D. Day and V. Borzenets for the TXM experiment at beamline 6-2C of SSRL is gratefully acknowledged.

ORCID

Rajendra K. Bordia  <https://orcid.org/0000-0001-9256-0301>

Yijin Liu  <https://orcid.org/0000-0002-8417-2488>

Kyle S. Brinkman  <https://orcid.org/0000-0002-2219-1253>

Wilson K. S. Chiu  <https://orcid.org/0000-0001-7402-4951>

REFERENCES

1. Ringwood AE, Kesson SE, Ware NG, Hibberson W, Major A. Immobilisation of high level nuclear reactor wastes in SYNROC. *Nature*. 1979;278(5701):219-23.

2. Kerr RA. Nuclear waste disposal: alternatives to solidification in glass proposed. *Science*. 1979;204(4390):289-91.
3. Ringwood AE, Kesson SE, Ware NG, Hibberson WO, Major A. The SYNROC process: a geochemical approach to nuclear waste immobilization. *Geochem J*. 1979;13:141-65.
4. Ringwood AE. Disposal of high-level nuclear wastes: a geological perspective. *Mineral Mag*. 1985;49(351):159-76.
5. Waste Forms Technology and Performance: Final report committee on waste forms technology and performance; National. 2011.
6. Amoroso J, Marra JC, Tang M, Lin Y, Chen F, Su D, et al. Melt processed multiphase ceramic waste forms for nuclear waste immobilization. *J Nucl Mater*. 2014;454(1-3):12-21.
7. Xu Y, Wen Y, Grote R, Amoroso J, Nickles LS, Brinkman KS. A-site compositional effects in Ga-doped hollandite materials of the form $BaxCsyGa_{2x+y}Ti_{8-2x-y}O_{16}$: implications for Cs immobilization in crystalline ceramic waste forms. *Sci Rep*. 2016;6(1):1-8.
8. Wang L, Liang T. Ceramics for high level radioactive waste solidification. *J Adv Ceram*. 2012;1(3):194-203.
9. Cocco AP, Nelson GJ, Harris WM, Nakajo A, Myles TD, Kiss AM, et al. Three-dimensional microstructural imaging methods for energy materials. *Phys Chem Chem Phys* [Internet]. 2013;15(39):16377-407. Available from <http://www.ncbi.nlm.nih.gov/pubmed/23897122>.
10. Brinkman K, Fox K, Marra J. Crystalline Ceramic Waste Forms: Reference Formulation Report. 2012;(February). Available from: <http://www.osti.gov/servlets/purl/1042587/>.
11. Ewing RC, Weber WJ, Lian J. Nuclear waste disposal-pyrochlore (A₂B₂O₇): Nuclear waste form for the immobilization of plutonium and "minor" actinides. *J Appl Phys*. 2004;95(11 D):5949-71.
12. Lumpkin GR. Ceramic waste forms for actinides. *Elements*. 2006;2(6):365-72.
13. Yudintsev SV, Stefanovsky SV, Nikonov BS. A pyrochlore-based matrix for isolation of the REE-actinide fraction of wastes from spent nuclear fuel reprocessing. *Dokl Earth Sci*. 2014;454(1):211-5.
14. Cocco AP, Degostin MB, Wrubel JA, Damian PJ, Hong T, Xu Y, et al. Three-dimensional mapping of crystalline ceramic waste form materials. *J Am Ceram Soc*. 2017;100:3722-3735.
15. Wilson JR, Kobsiriphat W, Mendoza R, Chen H-Y, Hiller JM, Miller DJ, et al. Three-dimensional reconstruction of a solid-oxide fuel-cell anode. *Nat Mater* [Internet]. 2006;5(7):541-4. Available from <http://www.nature.com/doi/10.1038/nmat1668>.
16. Shearing PR, Cai Q, Golbert JI, Yufit V, Adjiman CS, Brandon NP. Microstructural analysis of a solid oxide fuel cell anode using focused ion beam techniques coupled with electrochemical simulation. *J Power Sources* [Internet]. 2010;195(15):4804-10.
17. Vivet N, Chupin S, Estrade E, Piquero T, Pommier PL, Rochais D, et al. 3D Microstructural characterization of a solid oxide fuel cell anode reconstructed by focused ion beam tomography. *J Power Sources* [Internet]. 2011;196(18):7541-9.
18. Iwai H, Shikazono N, Matsui T, Teshima H, Kishimoto M, Kishida R, et al. Quantification of SOFC anode microstructure based on dual beam FIB-SEM technique. *J Power Sources*. 2010;195(4):955-61.
19. Ahmad M, Prax G, Bazalova M, Xing L. X-ray luminescence and X-ray fluorescence computed tomography : new molecular imaging modalities. *IEEE Access*. 2014;2:1051-61.
20. Grew KN, Chu YS, Yi J, Peracchio AA, Izzo JR, Hwu Y, et al. Nondestructive nanoscale 3D elemental mapping and analysis of a solid oxide fuel cell anode. *J Electrochem Soc*. 2010;157(6):B783.
21. Yin GC, Tang MT, Song YF, Chen FR, Liang KS, Duerwer FW, et al. Energy-tunable transmission x-ray microscope for differential contrast imaging with near 60 nm resolution tomography. *Appl Phys Lett*. 2006;88(24):8-11.
22. Henke BL, Gullikson EM, Davis J. X-ray interactions: photoabsorption, scattering, transmission, and reflection at E=50-30000 eV, Z = 1-92. *At Data Nucl Data Tables*. 1993;54(2):181-342.
23. Amoroso JW, Marra J, Dandeneau CS, Brinkman K, Xu Y, Tang M, et al. Cold crucible induction melter test for crystalline ceramic waste form fabrication: A feasibility assessment. *J Nucl Mater* [Internet]. 2017;486:283-97.
24. Liu Y, Meirer F, Williams PA, Wang J, Andrews JC, Pianetta P. TXM-Wizard: A program for advanced data collection and evaluation in full-field transmission X-ray microscopy. *J Synchrotron Radiat*. 2012;19:281-7.
25. Grew KN, Peracchio AA, Joshi AS, Izzo JR, Chiu W. Characterization and analysis methods for the examination of the heterogeneous solid oxide fuel cell electrode microstructure. Part 1: Volumetric measurements of the heterogeneous structure. *J Power Sources*. 2010;195(24):7930-42.
26. Grew KN, Peracchio AA, Chiu W. Characterization and analysis methods for the examination of the heterogeneous solid oxide fuel cell electrode microstructure: Part 2. Quantitative measurement of the microstructure and contributions to transport losses. *J Power Sources*. 2010;195(24):7943-58.

SUPPORTING INFORMATION

Additional supporting information may be found online in the Supporting Information section at the end of the article.

How to cite this article: Damian PJC, Cocco AP, Wrubel JA, et al. Simultaneous three-dimensional elemental mapping of Hollandite and Pyrochlore material phases in ceramic waste form materials. *J Am Ceram Soc*. 2019;102:5620-5631. <https://doi.org/10.1111/jace.16371>